

Aperiodicity, structure, and dynamics in $\text{Ni}(\text{CN})_2$ Andrew L. Goodwin,^{1,*} Martin T. Dove,¹ Ann M. Chippindale,² Simon J. Hibble,² Alexander H. Pohl,² and Alex C. Hannon³¹*Department of Earth Sciences, University of Cambridge, Downing Street, Cambridge CB2 3EQ, United Kingdom*²*Department of Chemistry, University of Reading, Whiteknights, Reading, Berkshire RG6 6AD, United Kingdom*³*ISIS Facility, Rutherford Appleton Laboratory, Chilton, Didcot, Oxfordshire OX11 0QX, United Kingdom*

(Received 11 June 2009; published 4 August 2009)

By combining the results of both x-ray diffraction and neutron total-scattering experiments, we show that $\text{Ni}(\text{CN})_2$ exhibits long-range structural order only in two dimensions, with no true periodicity perpendicular to its gridlike layers. Reverse Monte Carlo analysis gives an experimental distinction between M–C and M–N bond lengths in a homometallic cyanide framework and identifies the vibrational modes responsible for anomalous positive and negative thermal expansion in the title compound.

DOI: 10.1103/PhysRevB.80.054101

PACS number(s): 61.43.–j, 61.05.fg, 61.05.C–, 65.40.De

I. INTRODUCTION

One of the most appealing aspects of the cyanide ion as a coordinating ligand is its ability to promote the growth of low-dimensional crystalline phases through its linear coordination motif M–CN–M.^{1–8} Nickel(II) cyanide, $\text{Ni}(\text{CN})_2$, is a particularly topical example because it has been proposed as an inorganic analog of graphene,⁹ capable of forming intercalates^{10,11} and even nanotubular structures.⁹ Quite remarkably, however, key aspects of its crystal structure remain unknown. While it has been shown that each Ni^{2+} center is coordinated by four bridging cyanide ions to give two-dimensional square-grid layers,⁷ the arrangement of these layers in three dimensions remains controversial.^{7,12,13} Characterizing this arrangement is of critical importance because it holds the key to understanding the weak interactions between layers. Not only do these interactions dictate the material's intercalation behavior^{10,11} but, more generally, it is increasingly apparent that understanding and exploiting weak interactions is a promising approach to the design of materials with new and useful functionalities.^{14–16}

From a crystallographic viewpoint, the difficulty in obtaining a complete structural solution from diffraction data has always been due to the existence of both structured diffuse scattering and selective peak broadening effects [Fig. 1(a)]. Neutron total-scattering methods have enabled real-space modeling of the local structure via the experimental pair distribution function,^{7,17,18} and very good agreement in real space was obtained for a model in which the square-grid layers are stacked in a perpendicular direction at intervals of 3.20 Å.⁷ The same model also accounted for the sharp diffraction features in reciprocal space but was unable to reproduce the diffuse scattering or to predict the correct reflection conditions [Fig. 1(b)].

In this paper, we show that traditional crystallographic analysis fails because $\text{Ni}(\text{CN})_2$ is long-range ordered only in two dimensions, with no true long-range periodicity along a direction perpendicular to its gridlike layers. Instead the layers assume a disordered stacking arrangement—a type of structural description for transition-metal cyanides that we anticipate will help resolve a range of crystallographic ambiguities in the field.⁸ Our model reproduces all real-space and reciprocal-space neutron and x-ray diffraction data for

$\text{Ni}(\text{CN})_2$ and develops from simple chemical rules. We also use the reverse Monte Carlo (RMC) technique¹⁹ to produce atomistic models of $\text{Ni}(\text{CN})_2$, from which we extract key structural and dynamical correlations, including an experimental distinction between M–C and M–N bond lengths in a homometallic cyanide framework. This information will provide an important constraint in the development of models of $\text{Ni}(\text{CN})_2$ -based nanophases.⁹ Moreover, we identify the vibrational modes of $\text{Ni}(\text{CN})_2$ implicated in its strong positive thermal expansion (PTE) perpendicular to the square-grid layers and also its negative thermal expansion (NTE) within the layers themselves.

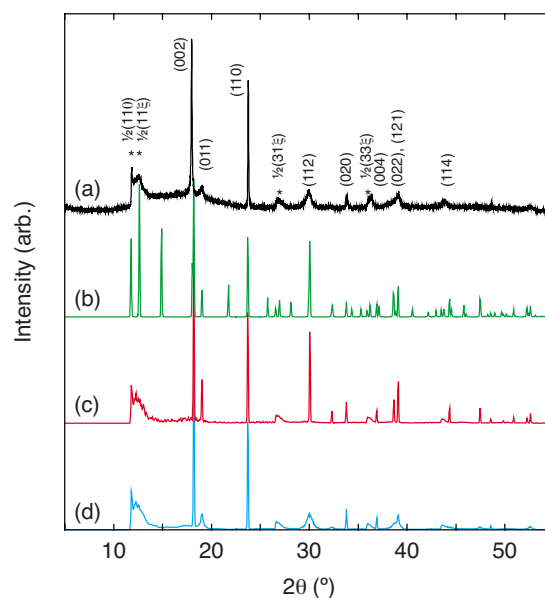


FIG. 1. (Color online) (a) Experimental and [(b)–(d)] calculated x-ray diffraction patterns for $\text{Ni}(\text{CN})_2$ [$\lambda=1.0000(1)$ Å]: (b) $P4_2/mmc$ model from Ref. 7; the new disordered stacking model, (c) without, and (d) with Gaussian shear distribution perpendicular to [001]. The superstructure and diffuse scattering peaks that arise from the disordered stacking along *c* are indicated by asterisks (see Appendix for derivation).

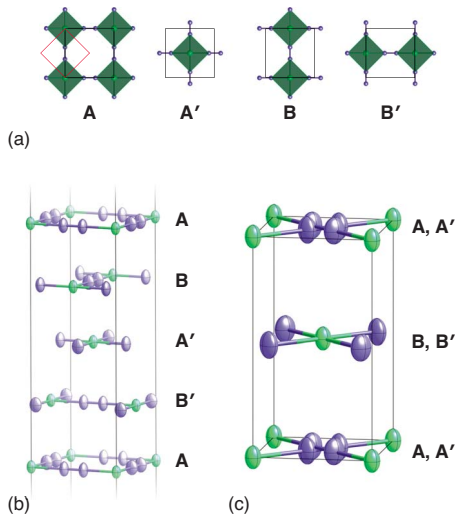


FIG. 2. (Color online) (a) The four possible square-grid orientations referred to in the text, (b) an example stacking sequence, and (c) the average structure $I4/mmm$ unit cell (whose relative orientation with respect to the axes in (a) is shown in red); thermal ellipsoids were calculated from the real-space RMC fits to the 298 K neutron data (Ref. 7) and are shown at the 50% probability level. Square planar Ni atoms in green; linearly-bridged C/N atoms in purple.

II. CRYSTALLOGRAPHIC MODEL

A. General features

Our crystallographic model develops from the basic stacking motif identified in Ref. 7; namely, that square-grid layers stack such that cyanide ions of one layer are positioned directly above Ni^{2+} cations of the layer below. Because there are twice as many CN groups as Ni atoms, there are two such arrangements for each pair of layers. As the number of layers increases so too does the number of possible stacking arrangements that satisfy this basic local constraint. Consequently, there are a large number of essentially degenerate structural ground states—each corresponding to a different stacking arrangement but with almost identical local structures (and hence lattice enthalpies). In this model, there is no long-range stacking periodicity of the type described in Ref. 7; instead the system is a “disordered stack” where true periodicity is lost in one crystallographic direction.

Like many disordered solids, this disordered stack exhibits a characteristic short-range order that reflects certain local constraints. First, there are only four possible orientations for any particular sheet [Fig. 2(a)], which we term A, A', B, and B'. The layers A or A' give the correct local environment when placed above B or B'-type layers but not when above A or A'-type layers; this gives a second constraint. So, the model divides the structure into “even” layers, with only A or A'-type sheets and “odd” layers containing B or B' sheets [an example is shown in Fig. 2(b)]. The $P4_2/mmc$ model of Ref. 7 is also consistent with these “rules” in that it corresponds to the specific four-layer repeat ABAB'.

The average unit cell for the disordered arrangement is a tetragonal cell in space group $I4/mmm$ [$a=3.434(3)$ Å and

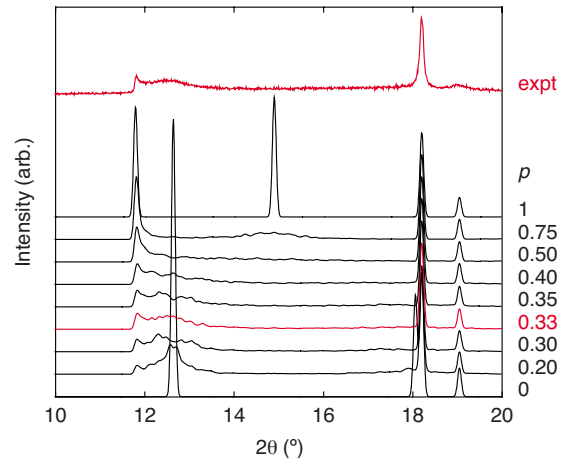


FIG. 3. (Color online) Experimental (top) and calculated x-ray diffraction patterns for $\text{Ni}(\text{CN})_2$ using different values of the second-layer correlation variable p .

$c=6.401(2)$ Å at 298 K], with Ni and C/N atoms of half occupancy at $(0,0,0)$ and $(x,x,0)$ ($x\sim 0.38$), respectively, [Fig. 2(c); see Appendix for crystallographic derivation]. The corresponding x-ray diffraction pattern, calculated using a random series of 200 layers that obey the aforementioned rules is illustrated in Fig. 1(c). One now finds the correct number of peaks and also the key diffuse features. Moreover, all cyanide groups are crystallographically equivalent in this cell, consistent with spectroscopic data.²⁰

B. Second-layer correlations

The form of the diffuse scattering near $2\theta=12.5^\circ$ is remarkably sensitive to correlations between second-nearest-neighbor layers. We define a second-layer correlation function p which gives the likelihood that second-nearest-neighbor layers are of the same type (i.e., a short-range-order parameter). This can take the values $0\leq p\leq 1$, where $p=0$ corresponds to the unique ordering pattern $[ABA'B']AB\dots$ (symmetry $I4_1/amd$, $a=4.9$ Å, $c=12.8$ Å), $p=1/2$ describes a purely statistical distribution of layer pairs, and $p=1$ corresponds to the two-layer repeat $[AB]AB\dots$ (symmetry $Cmmm$, $a=c=4.9$ Å, $b=6.4$ Å).

Structural models containing 200 layers for a range of different p values give very different x-ray powder-diffraction patterns; this difference is most noticeable in the form of the diffuse scattering between 2θ angles of 12 and 16° (Fig. 3). At low values of p —i.e., less than 0.33—the calculated diffraction pattern cannot reproduce the sharp peak seen just below 12° in 2θ while the bunching of diffuse intensity near $2\theta=12.5^\circ$ is reproduced. For $0.33<p<0.50$, the sharp feature becomes very prominent but the diffuse scattering is increasingly spread out. At values of p greater than 0.50, the diffuse scattering centers around a new 2θ angle of about 15° . The calculated diffraction pattern that gives the most reasonable qualitative fit to the observed data is for $p=0.33$. It can be seen from Fig. 3 that the diffraction pattern changes rapidly with p , giving a rough estimate of an error of ± 0.02 on the value of p we have determined. Note

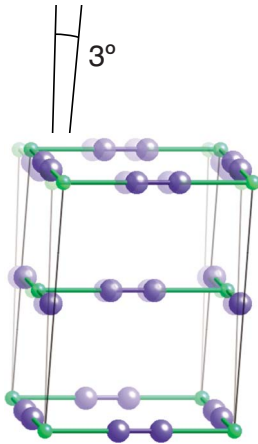


FIG. 4. (Color online) Illustration of the sideways displacements of $\text{Ni}(\text{CN})_2$ layers involved in the shear strain.

that the $p=0.33$ diffraction pattern given in Fig. 3 is precisely that shown in Fig. 1(c).

A value of $p=0.33$ indicates that the probability of finding like pairs of even (e.g., $A\dots A$) or odd (e.g., $B\dots B$) layers is 0.33 while the probability of finding unlike pairs is 0.67—about twice as great. This preference for different pairs at the second-layer distance may arise in order to avoid cyanide groups being bound simultaneously to Ni^{2+} centers in both adjacent sheets. It is possible that the actual value of p for a given sample may be highly dependent on sample preparation and history.

C. Shear displacements

To complete the modeling of the diffraction pattern in Fig. 1(a), the strong peak-broadening effects observed for general (hkl) reflections are accounted for in terms of a shear distribution perpendicular to $[001]$ —i.e., concerted sideways displacement of the layers, facilitated by the very weak inter-layer forces (Fig. 4). Such a shear term preserves $(hk0)$ and $(00l)$ reflections but broadens composite (hkl) reflections—e.g., the (112) reflection at $2\theta \approx 30^\circ$. Our models of shear strain distributions use a distribution of triclinically distorted variants of the $p=0.33$ disordered stacking model described above. Unit-cell angles vary such that $\alpha=90^\circ-\delta$, $\beta=90^\circ-\frac{\delta}{2}$, and $\gamma=90^\circ$ for a range of angles $-6^\circ < \delta < 6^\circ$, hence simulating shear along the $[120]$ direction.²¹ Qualitative agreement with the experimental data is best achieved for a Gaussian distribution in δ with width 2.5° , corresponding to an actual deviation of the c axis of $2.8^\circ \approx 3^\circ$ from its original orientation and a sideways displacement of successive layers of 0.16 \AA ; the calculated diffraction pattern is shown in Fig. 1(d).

D. Neutron diffraction pattern

As a final check of the validity of our structural model, we calculated the expected neutron-scattering pattern for the same structural model (stacking sequence, shear distribution) as that used to generate the x-ray pattern in Fig. 1(d). The calculated and experimental neutron-diffraction patterns are

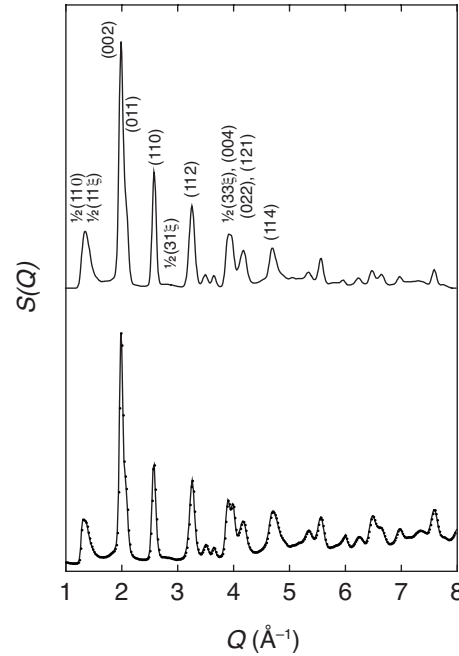


FIG. 5. Calculated (top) and experimental (bottom) neutron-scattering patterns.

illustrated in Fig. 5; clearly there is a good qualitative match between the two.

III. RMC ANALYSIS

A. Methodology

Quantitative fits to both real- and reciprocal-space neutron total-scattering data²² were obtained via RMC refinement of atomic displacements in a large supercell of the crystallographic unit cell.¹⁹ Parallel RMC refinements were performed using starting configurations based on both the (new) disordered stacking model and the original $P4_2/mmc$ model of Ref. 7. Each RMC configuration contained 64 000 atoms and represented a box approximately 100 \AA in each direction. The refinement process itself was driven by fitting to both real-space and reciprocal-space neutron-scattering data collected on the GEM instrument²² at ISIS, in the form of the $T(r)$ and $QF(Q)$ functions, respectively.²³ Both models are capable of producing excellent fits to real-space data [Fig. 6(a)]; however, the quality of the corresponding reciprocal-space fits [Fig. 6(b)] and the feasibility of the atomic distributions (see below) were both improved for the disordered stacking model. It was not computationally feasible to include the shear contribution in these calculations—this omission is responsible for some “ringing” in the $QF(Q)$ difference curves.

A slight difference in the physical viability of the real-space models obtained for both the “random stacking” and $P4_2/mmc$ regimes can be seen by collapsing representative RMC configurations onto the smallest common unit cell of the two models: namely, the $4.9 \text{ \AA} \times 4.9 \text{ \AA} \times 12.8 \text{ \AA}$ cell of the $P4_2/mmc$ model. Views of these “collapsed” configurations are given in Fig. 7. What one is looking to check in

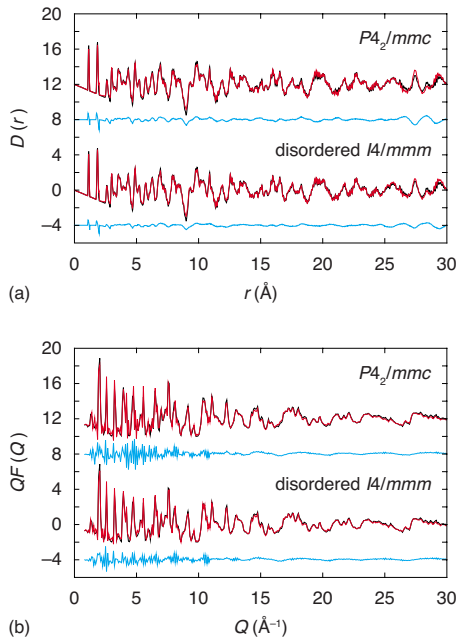


FIG. 6. (Color online) RMC fits (red lines) to (a) $D(r)$ and (b) $QF(Q)$ neutron data (black lines) using the $P4_2/mmc$ (upper set in each panel; shifted by 12 units) and disordered $I4/mmm$ (bottom set in each panel) models; difference curves (data–fit; shifted by 4 units) shown in blue.

these distribution plots is whether the individual atomic distributions make physical sense. In the case of the random stacking model, the Ni distributions are all essentially equivalent, as are the various C/N distributions [Figs. 7(a) and 7(b)]. For the $P4_2/mmc$ model, one finds that RMC has been forced to introduce some spurious atomic distributions. The C/N distributions at a cell height of $\frac{1}{4}$ and $\frac{3}{4}$, for example, adopt teardroplike shapes, that are not symmetric with respect to the corresponding Ni(CN)₂ layer [Fig. 7(c)]. That is, the model requires CN out-of-plane vibrations to take different energies for translations in one direction (“up”) than in the other direction (“down”), which is unlikely from a chemical viewpoint. There are also clear differences between CN molecules located at different points of the unit cell; for example, in the layer at height $z = \frac{1}{2}$ [Fig. 7(d)] one of the CN molecules has very isotropic C and N displacements while the other CN molecule in this same layer has highly anisotropic displacements. This again would be expected to give rise to a splitting in the CN stretching frequencies, which is not observed experimentally.

Consequently, while the difference between the two models is primarily one of periodicity, these are indicators that

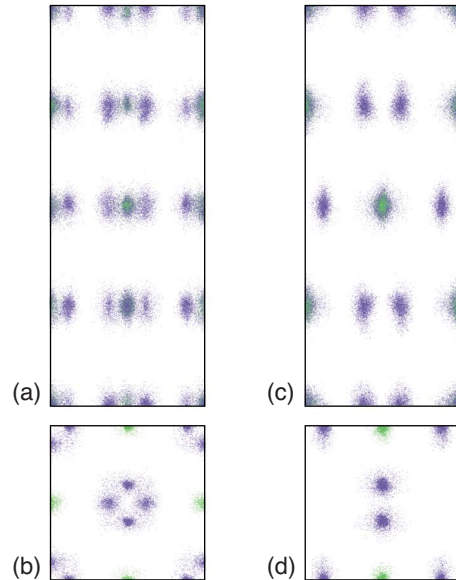


FIG. 7. (Color online) RMC atomic positional distributions obtained by “collapsing” equilibrium RMC configurations onto a single cell of the $P4_2/mmc$ model: (a) and (b) are from the random stacking model, viewed down $[010]$ and $[001]$, respectively; (c) and (d) are for the $P4_2/mmc$ model viewed down $[010]$ and $[001]$, respectively. In both (b) and (d) only the single sheet near $z = \frac{1}{2}$ is shown.

the local structure is also better represented by the disordered model. The corresponding crystallographic parameters for this model, obtained by collapsing the RMC configurations onto a single $I4/mmm$ unit cell, are summarized in Table I. Anisotropic displacement parameters were calculated from the observed mean-squared displacements from the average positions; estimated standard errors were calculated from the observed second (x) and fourth (U_{ij}) distribution moments.²⁴

B. Metal–C/N bond lengths

Having shown our random stacking RMC configurations to provide reliable atomistic models of Ni(CN)₂, we address a long-standing problem in the crystallography of homometallic transition-metal cyanide frameworks: namely, whether the metal–C and metal–N bonds have different lengths.^{1–8} Our real-space configurations do show a reproducible difference in Ni–C and Ni–N bond lengths [1.880(9) and 1.834(9) Å, respectively]. Moreover, when we interchange C and N atoms in our configurations, further refinement also interchanges the mismatched bond lengths so that the same average values are obtained again on convergence (Fig. 8).

TABLE I. $I4/mmm$ Ni(CN)₂ crystallographic parameters determined from RMC analysis of neutron total-scattering data collected at 298 K. Anisotropic displacement parameters in Å²; $U_{22}=U_{11}$; $U_{13}=U_{23}=0$.

Atom	x	y	z	Occ.	U_{11}	U_{12}	U_{33}
Ni	0	0	0	0.5	0.0219(3)	0	0.0493(6)
C	0.3866(19)	x	0	0.25	0.0315(6)	–0.0104(6)	0.0655(7)
N	0.3773(19)	x	0	0.25	0.0319(6)	–0.0111(6)	0.0664(7)

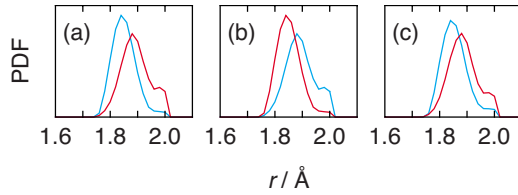


FIG. 8. (Color online) Ni–C (red) and Ni–N (blue) distributions in $\text{Ni}(\text{CN})_2$ (a) from the original RMC refinements, (b) after swapping N and C atoms without further refinement, and (c) after subsequent RMC minimization.

The sensitivity here comes from the different neutron-scattering lengths of the C and N atoms, amplified further by fitting in real space. That the M–N bond is slightly shorter is perhaps counterintuitive but is actually in accordance with DFT calculations for $\text{Zn}(\text{CN})_2$ and $\text{Cd}(\text{CN})_2$.²⁵ Our final average structure model, obtained by collapsing the RMC configuration onto a single $I4/mmm$ unit cell, gives C and N atom positions $(x, x, 0)$ of $x=0.3866(19)$ and $0.3773(19)$, respectively.

These distributions also address the issue of CN ordering in $\text{Ni}(\text{CN})_2$. Based on the observation that all homometallic cyanide frameworks exhibit cyanide orientational disorder, the cyanide orientations in our RMC configurations were assigned randomly and the Ni–CN–Ni connectivity fixed during RMC refinement. If the square-grid layers are, in fact, assembled from alternating $[\text{NiC}_4]$ and $[\text{NiN}_4]$ centers, then because our neighbor constraints in *RMCProfile* prevented “flipping” of the cyanide groups, the best compromise available during refinement is to place the N atoms at the Ni–C distance for “ $[\text{NiC}_4]$ ”-type Ni atoms and the C atoms at the Ni–N distance for “ $[\text{NiN}_4]$ ”-type Ni atoms. This would give similar, bimodal distributions for the Ni–C and Ni–N bond lengths when averaged over the configuration, which is not what we observe in Fig. 8. Hence, that we have distinguishable unimodal distributions indicates both that the RMC fitting process would be sensitive CN ordering and also that no such ordering is evident in the scattering data.

C. Lattice dynamics

Addressing now the NTE/PTE effects in $\text{Ni}(\text{CN})_2$,⁷ we calculate the phonon spectrum from our RMC configurations using the method described in Refs. 26 and 27. The lack of periodicity along \mathbf{c} means that vibrations with \mathbf{c}^* wave-vector components are not well described in terms of a classical phonon model. However the lattice vibrations of individual layers (i.e., with periodicities confined to the $(001)^*$ plane of reciprocal space) can certainly be determined.^{26,27}

We find a total of five dispersionless phonon modes with frequencies below 1.0 THz (4.1 meV), each of which corresponds to a localized mode of the $\text{Ni}(\text{C/N})_4$ square units (Fig. 9). Four of these modes are rigid unit modes²⁸ but the existence of a fifth low-frequency mode that involves bending of the cyanide–Ni–cyanide bonds implies that the $\text{Ni}(\text{C/N})_4$ square units are less rigid than might have otherwise been thought. All five modes result in decreasing Ni...Ni separations with increasing temperature and so con-

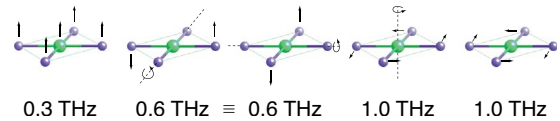


FIG. 9. (Color online) Lowest-energy dispersionless vibrational modes in $\text{Ni}(\text{CN})_2$.

tribute to NTE within the square-grid layers. Moreover, the very lowest-energy modes involve translations perpendicular to the square-grid layers, driving the very large positive thermal expansion in this direction as suggested in Ref. 7.

IV. CONCLUSIONS

In conclusion, we have determined the complete structure of $\text{Ni}(\text{CN})_2$, showing that the material is truly periodic in only two dimensions; the stacking sequence of square-grid $\text{Ni}(\text{CN})_2$ layers obeys simple chemical rules driven by apical coordination of the $d^8 \text{Ni}^{2+}$ centers but these rules are insufficient to give long-range periodicity along the stacking direction. The weak interlamellar interactions give rise to two-dimensional lattice dynamics, strong PTE along the tetragonal axis, and facilitate the formation of intercalate derivatives. We note that the availability of multiple Ni oxidation states then leaves open the possibility of forming graphenelike electronically active intercalate materials based on $\text{Ni}(\text{CN})_2$.

ACKNOWLEDGMENTS

The authors thank D. Palmer (CrystalMaker Software Ltd) for custom changes to CrystalDiffract. Financial support from Trinity College, Cambridge and the EPSRC (Research Fellowships for A.L.G.) is gratefully acknowledged. We also acknowledge the University of Cambridge’s CamGrid infrastructure for computational resources.

APPENDIX: RECIPROCAL LATTICE OF THE “DISORDERED STACKING” MODEL

An ordered stacking model in which each Ni atom of one layer is placed directly above another Ni atom of the layer below can be thought of as the convolution of a single $\text{Ni}(\text{CN})_2$ square-grid layer with the set of points $\rho(\mathbf{r}) = \sum_w \delta(\mathbf{r} - W\mathbf{c})$, where c is the interlayer separation (≈ 3.2 Å). For the disordered stacking model the stacking function $\rho(\mathbf{r})$ is given by

$$\rho(\mathbf{r}) = \sum_w \delta \left[\mathbf{r} - \left(\left\{ \frac{1}{4} [1 - (-1)^w] + \frac{\sigma_w}{2} \right\} \mathbf{a} + \frac{\sigma_w}{2} \mathbf{b} + W\mathbf{c} \right) \right], \quad (1)$$

where \mathbf{a} and \mathbf{b} are the unit-cell vectors for the square-grid layer, and $\sigma_w=0$ or 1 is assigned at random. Then the Fourier transform of the crystal $F_{\text{crystal}}(\mathbf{Q})$ is given by the expression

$$F_{\text{crystal}}(\mathbf{Q}) = F_{\text{layer}}(\mathbf{Q}) \times \sum_W \exp \left[i\mathbf{Q} \cdot \left(\left\{ \frac{1}{4} [1 - (-1)^W] + \frac{\sigma_W}{2} \right\} \mathbf{a} + \frac{\sigma_W}{2} \mathbf{b} + W\mathbf{c} \right) \right]. \quad (2)$$

Because an individual $\text{Ni}(\text{CN})_2$ layer is a primitive square grid, then $F_{\text{layer}}(\mathbf{Q})$ is a set of one-dimensional (1D) rods at $\mathbf{Q} = h\mathbf{a}^* + k\mathbf{b}^* + \chi\mathbf{c}^*$ ($h, k \in \mathbb{Z}; \chi \in \mathbb{R}$). The interesting term is the second term on the right-hand side of Eq. (2), which we call $F_{\text{stack}}(\mathbf{Q})$ and expand for general $\mathbf{Q} = (hkl)$,

$$F_{\text{stack}}(\mathbf{Q}) = \sum_W \left[\exp \left(2\pi i \left\{ \frac{h}{4} [1 - (-1)^W] \right\} \right) \times \exp(2\pi i l W) \exp[\pi i \sigma_W (h+k)] \right]. \quad (3)$$

If $(h+k)$ is even then the “random” term $\exp[\pi i \sigma_W (h+k)]$ is equal to unity irrespective of the individual σ_W values; the sum is well behaved and we obtain nonzero $F_{\text{stack}}(\mathbf{Q})$ values only for h even, l integral, or h odd, $l/2$ odd. Note that the existence of reciprocal-lattice points at $l/2$ values immediately tells us that the real-space periodicity along \mathbf{c} involves two layers.

If $(h+k)$ is odd then the sum is not at all well behaved and we obtain nonzero values of $F_{\text{stack}}(\mathbf{Q})$ for arbitrary nonintegral l ; the term $\exp[\pi i \sigma_W (h+k)]$ equals 1 or -1 , and the lattice sums over W no longer vanish but scale with the square root of the number of layers. A schematic representation of the set of reciprocal-lattice points constructed in this way is given in Fig. 10(a). The conventional indexing of reciprocal space gives a face-centered tetragonal reciprocal cell with reciprocal-lattice vectors \mathbf{a}^* and \mathbf{b}^* at angles of 45° to the original choice of vectors \mathbf{a} and \mathbf{b} . The reciprocal-lattice vector \mathbf{c}^* corresponds to a real-space “periodicity” of two square-grid layers. Columns of 1D diffuse scattering are

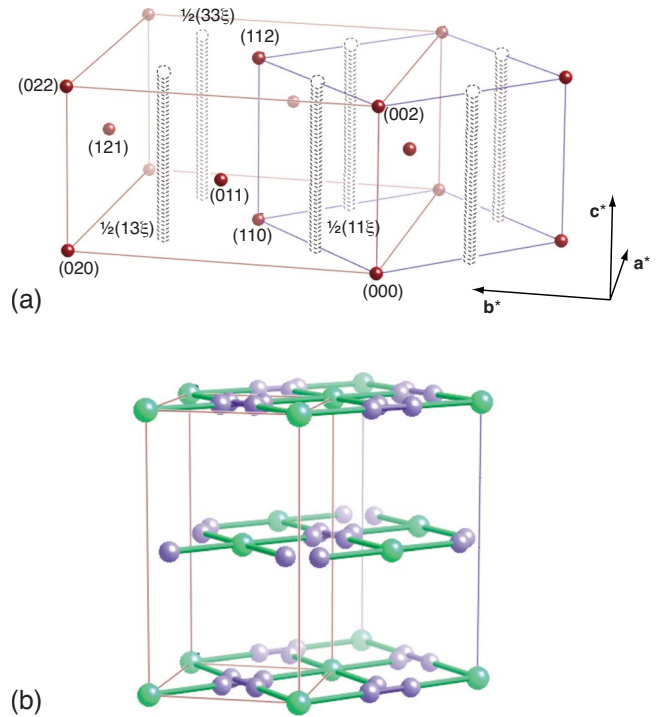


FIG. 10. (Color online) (a) Reciprocal-space and (b) real-space unit cells in $\text{Ni}(\text{CN})_2$. In both cases, the red cell corresponds to the standard crystallographic setting, and the blue cell is given to coincide with the primitive square lattice of an individual $\text{Ni}(\text{CN})_2$ sheet. Columns of diffuse scattering are predicted for reciprocal-lattice vectors $\mathbf{Q} = \frac{1}{2}(hk\xi)$ (h, k odd).

predicted to occur at $\mathbf{Q} = \frac{1}{2}(hk\xi)$ (h, k odd): these are responsible for the unusual peak shapes in the powder-diffraction pattern.²⁹

The real-space unit cell that corresponds to this choice of reciprocal-lattice vectors is a body-centered tetragonal cell, again with basal-plane vectors at 45° to the Ni–CN–Ni linkages; the relationship is illustrated in Fig. 10(b).

*alg44@cam.ac.uk

¹S. J. Hibble, S. M. Cheyne, A. C. Hannon, and S. G. Eversfield, *Inorg. Chem.* **41**, 4990 (2002).

²S. J. Hibble, S. M. Cheyne, A. C. Hannon, and S. G. Eversfield, *Inorg. Chem.* **41**, 1042 (2002).

³J. Wang, M. F. Collins and G. P. Johari, *Phys. Rev. B* **65**, 180103(R) (2002).

⁴S. J. Hibble, A. C. Hannon, and S. M. Cheyne, *Inorg. Chem.* **42**, 4724 (2003).

⁵J. T. Culp, J.-H. Park, F. Frye, Y.-D. Huh, M. W. Meisel, and D. R. Talham, *Coord. Chem. Rev.* **249**, 2642 (2005).

⁶R. Lescouëzec, L. M. Toma, J. Vaissermann, M. Verdagner, F. S. Delgado, C. Ruiz-Pérez, F. Lloret, and M. Julve, *Coord. Chem. Rev.* **249**, 2691 (2005).

⁷S. J. Hibble, A. M. Chippindale, A. H. Pohl, and A. C. Hannon, *Angew. Chem., Int. Ed.* **46**, 7116 (2007).

⁸A. G. Sharpe, *The Chemistry of Cyano Complexes of the Transition Metals* (Academic, London, England, 1976).

⁹Y. Mo and E. Kaxiras, *Small* **3**, 1253 (2007).

¹⁰Y. Mathey and C. Mazières, *J. Phys. (France) Lett.* **36**, 243 (1975).

¹¹S. M. Alonso and F. Aragón de la Cruz, *An. Quim. B* **79**, 62 (1983).

¹²A. Vegas, *An. Quim.* **70**, 214 (1974).

¹³F. Aragón de la Cruz and S. M. Alonso, *An. Quim. B* **76**, 306 (1980).

¹⁴A. L. Goodwin, M. Calleja, M. J. Conterio, M. T. Dove, J. S. O. Evans, D. A. Keen, L. Peters, and M. G. Tucker, *Science* **319**, 794 (2008).

¹⁵A. L. Goodwin, D. A. Keen, and M. G. Tucker, *Proc. Natl. Acad. Sci. U.S.A.* **105**, 18708 (2008).

¹⁶A. L. Goodwin, B. J. Kennedy, and C. J. Kepert, *J. Am. Chem.*

- Soc. **131**, 6334 (2009).
- ¹⁷S. J. Hibble, A. C. Hannon, and I. D. Fawcett, *J. Phys.: Condens. Matter* **11**, 9203 (1999).
- ¹⁸S. J. L. Billinge and M. G. Kanatzidis, *Chem. Commun. (Cambridge)* **2004**, 749.
- ¹⁹M. G. Tucker, D. A. Keen, M. T. Dove, A. L. Goodwin, and Q. Hui, *J. Phys.: Condens. Matter* **19**, 335218 (2007).
- ²⁰M. F. Amr El-Sayed and R. K. Sheline, *J. Inorg. Nucl. Chem.* **6**, 187 (1958).
- ²¹Shear strains with component along only one of the basal plane axes (i.e., parallel to [100] or [010]) do not reproduce all the observed broadening features.
- ²²A. C. Hannon, *Nucl. Instrum. Methods Phys. Res. A* **551**, 88 (2005).
- ²³D. A. Keen, *J. Appl. Crystallogr.* **34**, 172 (2001).
- ²⁴J. D. Valentine and A. E. Rana, *IEEE Trans. Nucl. Sci.* **43**, 2501 (1996).
- ²⁵P. Ding, E. J. Liang, Y. Jia, and Z. Y. Du, *J. Phys.: Condens. Matter* **20**, 275224 (2008).
- ²⁶A. L. Goodwin, M. G. Tucker, M. T. Dove, and D. A. Keen, *Phys. Rev. Lett.* **93**, 075502 (2004).
- ²⁷A. L. Goodwin, M. G. Tucker, E. R. Cope, M. T. Dove, and D. A. Keen, *Phys. Rev. B* **72**, 214304 (2005).
- ²⁸A. L. Goodwin, *Phys. Rev. B* **74**, 134302 (2006).
- ²⁹Note that this condition is equivalent to $(h+k)$ odd with respect to the original choice of **a** and **b** parallel to Ni–CN–Ni linkages.